

GEOPHYSICS

Untangling the environmental and tectonic drivers of the Noto earthquake swarm in Japan

Qing-Yu Wang^{1*†}, Xin Cui¹, William B. Frank¹, Yang Lu², Takashi Hirose³, Kazushige Obara⁴

The underlying mechanism of the ongoing seismic swarm in the Noto Peninsula, Japan, which generates earthquakes at 10 times the average regional rate, remains elusive. We capture the evolution of the subsurface stress state by monitoring changes in seismic wave velocities over an 11-year period. A sustained long-term increase in seismic velocity that is seasonally modulated drops before the earthquake swarm. We use a three-dimensional hydromechanical model to quantify environmentally driven variations in excess pore pressure, revealing its crucial role in governing the seasonal modulation with a stress sensitivity of 6×10^{-9} per pascal. The decrease in seismic velocity aligns with vertical surface uplift, suggesting potential fluid migration from a high-pore pressure zone at depth. Stress changes induced by abnormally intense snow falls contribute to initiating the swarm through subsequent perturbations to crustal pore pressure.

INTRODUCTION

Since late 2020, a swarm of crustal earthquakes in the northeastern region of the Noto Peninsula, Japan, far from the plate boundaries of the subducting Pacific and Philippine plates, has been responsible for hundreds of earthquakes per day. Unlike typical subduction zone interplate earthquakes, inland crustal earthquakes in Japan islands predominantly take place at relatively shallow depths [≤ 10 km; Japan Meteorological Agency (JMA)]. Earthquake locations show that the Noto earthquake swarm started at a depth of about 15 km, deeper than typical crustal earthquakes, and has since slowly migrated northeast toward the surface (Fig. 1). This distinct spatiotemporal pattern suggests that, rather than inter-earthquake stress interactions, there is an underlying forcing that is driving the earthquakes in the swarm to failure (1).

Regional GNSS (Global Navigation Satellite System) positioning suggests a volumetric increase of $\sim 1.4 \times 10^7 \text{ m}^3$ in the first 3 months of the swarm, suggesting that fluid migration may be the cause of the Noto earthquake swarms (2). Amezawa *et al.* (3) assert that crustal earthquake swarms exhibit distinct spatiotemporal patterns of earthquake migration, characterized by clusters that originate at depth and migrate upward, suggesting the presence of fluids as the driving factor behind such swarms; in the case of Noto, the source of such crustal fluids is likely from a concealed magma system (4) or slab-derived fluids (5). A three-dimensional (3D) analysis of seismic velocity structure (6) reveals a low-velocity zone beneath the Noto Peninsula, indicative of a localized zone of high pore pressure caused by fluids dehydrated from the subducted Pacific plate to the source region of the overlying crustal earthquake swarm.

Seismic wave velocities are sensitive to subtle changes in physical properties of the medium (7), particularly in porous regions such as volcanic systems and fault zones (8). The monitoring of seismic wave velocities with continuous ambient seismic noise has thus proven effective in tracking variations caused by both stress perturbations resulting from earthquakes (9–14) as well as from

environmental perturbations often associated with variations in pore fluid pressure (13, 15).

We measure continuous seismic velocity changes beneath the Noto Peninsula over more than a decade to capture the evolution of seismic velocity in the subsurface within the source region of the ongoing earthquake swarm. Tracking continuous seismic velocity changes allows us to examine how the crustal medium evolves before (16) and during the earthquake swarm (17) and whether these changes are consistent with local geodetic observations (18). To disentangle the environmental contributions to the observed changes in seismic velocity, we develop a physical model that incorporates local environmental forcings to quantitatively capture the evolution of excess pore pressure in the subsurface. Our modeling results reproduce the observed seasonal variations in seismic velocities, indicating that seismic velocity changes are strongly influenced by changes in local snow and rain fall, air pressure, and sea-level changes. The decrease in seismic velocity at depth starts coincidentally with the initiation of the earthquake swarm and continues until the daily number of earthquake tends to stabilize. We attribute this velocity decrease to the likely ascent of fluids at depth from the high-pore pressure zone to the overlying earthquake source region, where the swarm is then triggered by changes in excess pore pressure caused by intense seasonal snow fall.

RESULTS

Recent earthquake swarm beneath the Noto Peninsula

The Noto Peninsula (Fig. 1A) is located along the Japan Sea on the west coast of Honshu, the largest island of Japan. The ongoing earthquake swarm is occurring in the northeastern region of the Noto Peninsula, migrating from its initiation in the south to the northeast since late 2020. Earthquakes in this swarm locate to relatively shallow depths, typically ranging from the near subsurface to 15 km (Fig. 1, B and C) (6). The estimated focal mechanisms of relatively large earthquakes align with existing reverse faults (3).

We first focus on how the temporal distribution of earthquakes (Fig. 2A), indicative of what drives them to rupture, changes throughout our observational period. During the swarm, we observe a multi-year cluster-like pattern with shorter inter-event times. The seismic activity during this period is organized in time into distinct clusters

Copyright © 2024 The Authors, some rights reserved; exclusive licensee American Association for the Advancement of Science. No claim to original U.S. Government Works. Distributed under a Creative Commons Attribution NonCommercial License 4.0 (CC BY-NC).

¹Department of Earth, Atmospheric and Planetary Sciences, Massachusetts Institute of Technology Cambridge, MA, USA. ²Department of Meteorology and Geophysics, University of Vienna, Vienna, Austria. ³Department of Geophysics, Graduate School of Science, Tohoku University, Sendai, Japan. ⁴Earthquake Research Institute, University of Tokyo, Bunkyo, Tokyo, Japan.

*Corresponding author. Email: qingyuwa@mit.edu

†Present address: University Grenoble Alpes, CNRS, ISTerre, Grenoble, France.

of events, suggesting that there is an underlying process driving the earthquakes to failure rather than the typical inter-source stress interaction, including both static and dynamic stress perturbations (19), that governs aftershock sequences (20, 21). Before the swarm (Fig. 2A), the earthquake activity resembles a random sequence of uncorrelated events. We quantify this observed difference in the behavior of earthquake timing by comparing the temporal distribution of earthquakes before and during the swarm (Fig. 2B).

We do this by computing the power spectral density of the earthquake histogram through time during these periods, as shown in Fig. 2C. During the time period before the swarm, the flat power spectrum is representative of a random Poisson-like distribution of seismicity that exhibits no correlation in time (20). During the swarm, the amplitude of the power spectrum increases proportionally with the period, indicating a clustering of seismic events over a broad range of timescales. The linear slope of the spectrum (in logarithmic space and thus representative of a power law) is larger than 1, suggesting a strong correlation of events in time (20). These results provide evidence supporting the hypothesis that swarm events differ from pre-swarm events and are triggered by an underlying

process that connects the timing of spatially disparate earthquakes to produce a strong correlation in the event occurrence.

Monitoring seismic velocity changes in the crust

To capture the signature of the crustal processes driving the earthquake swarm, we monitor the temporal changes in seismic velocity among three station pairs located near the earthquake swarm through coda wave interferometry using data from the high-sensitivity seismograph network (Hi-net) (22, 23). We analyze the seismic data within two distinct period ranges: 2 to 4 s and 4 to 10 s. We observe that changes in seismic velocity in both period ranges are primarily influenced by seasonal effects present at all the station pairs (fig. S2). These effects are characterized by a decrease in velocity during the winter months and an increase during the summer months. These observations remain consistent across multiple period ranges and align with previous research findings along the western coast of Japan (24).

In addition to the seasonal effects evident in both long- and short-period measurements, we observe a long-term increase in the seismic wave velocity followed by a decrease at depth, revealed by the longer-period 4- to 10-s measurement from the YGDH-SUZH

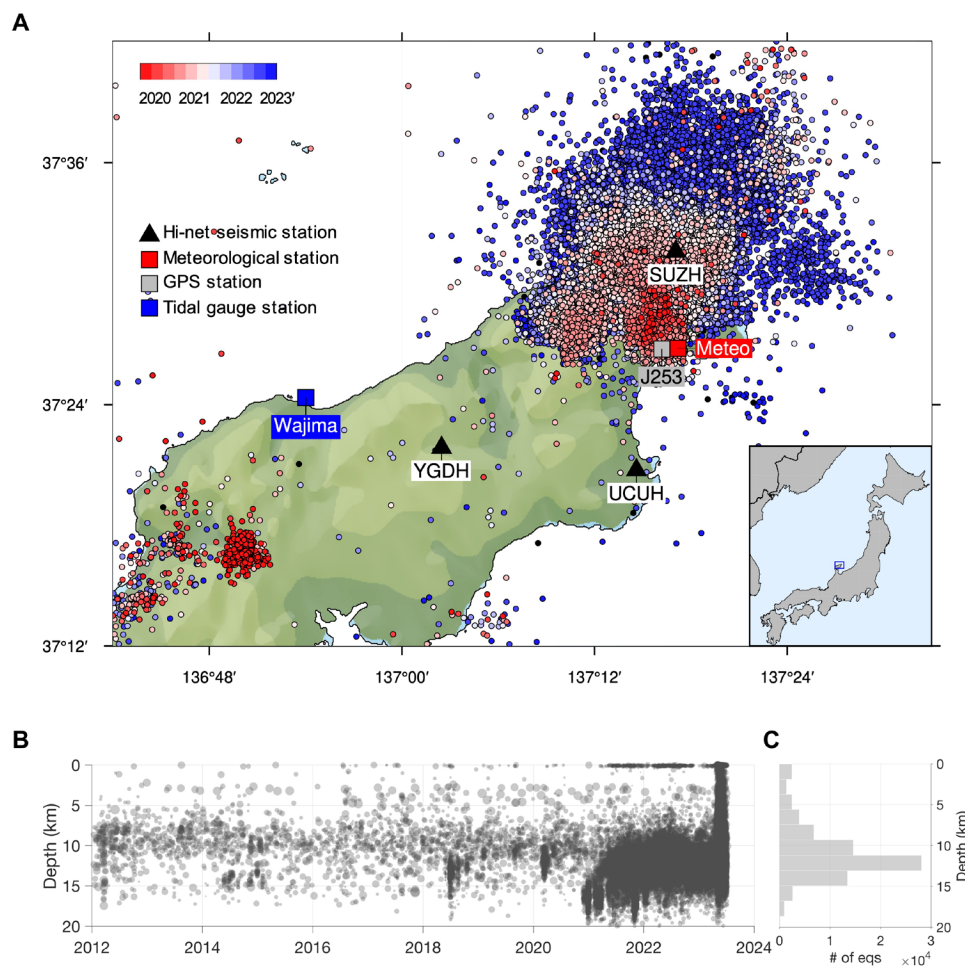


Fig. 1. Earthquake swarms and the seismic network in Noto, Japan. (A) Spatial distribution of earthquakes ($M_v \geq 2$, velocity magnitude estimated by the JMA) from 2020 to 2023 (JMA catalog). (B) Depth distribution of earthquakes through time. (C) Distribution of earthquake depths.

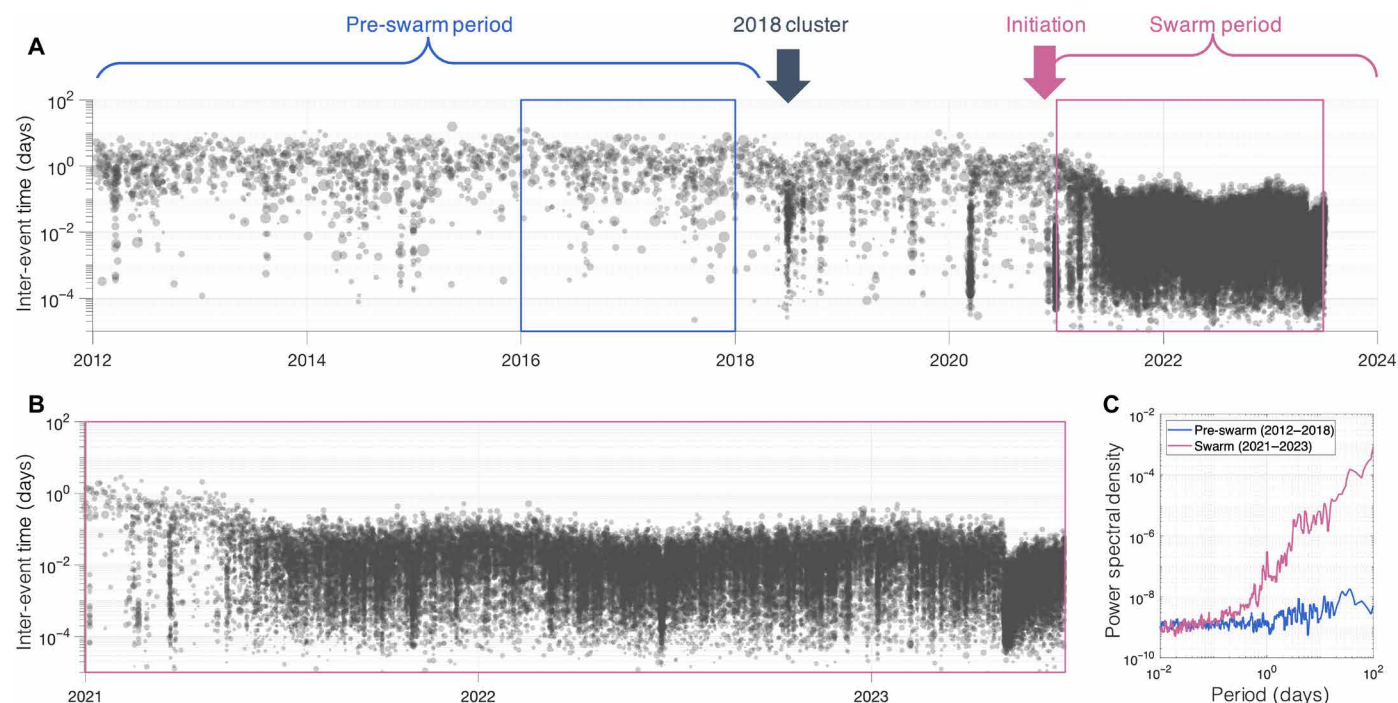


Fig. 2. Clustered timing of earthquakes during the Noto swarm. (A) Earthquake inter-event times that are evaluated during a pre-swarm (blue rectangle) and swarm periods (pink rectangle). (B) Zoom on the time period of the Noto swarm [pink rectangle in (A)]. (C) Power spectral density of earthquake timing during the pre-swarm (blue) and swarm periods (pink).

station pair, whose path crosses through the earthquake swarm (Fig. 1). This result is suggestive of long-term subsurface deformation in the source region of the swarm, perhaps along preexisting reverse faults in the northeastern region of the peninsula, as proposed by (25). The seismic monitoring results obtained from the remaining station pairs do not exhibit a distinct long-term trend before the occurrence of the earthquake swarm, nor do they demonstrate a change preceding the onset of the swarm. The interstation ray path between SUZH and UCUH traverses both land and ocean, introducing additional complexity to wave propagation and potentially leading to higher measurement uncertainties. We also note that the local *S*-wave structure (6) beneath the SUZH-UCUH station pair is not witness to the pronounced high-pore fluid pressure zone that is evident beneath the YGDH-SUZH station pair. The YGDH-UCUH station pair, whose path does not cross through the earthquake swarm, exhibits clear seasonal modulation with no discernible similar long-term trend.

Hydromechanical model of pore fluid pressure

With apparent seasonal and tectonic contributions to subsurface seismic velocities, it is necessary to disentangle the two contributors to seismic velocity changes observed here. Past work has highlighted that hydrologic loading due to meteorological and oceanographic effects can induce seasonal variations in crustal seismic velocities in Japan (24). We use a 3D fully coupled hydromechanical model to simulate the evolution of excess pore pressure (P_p) due to these environmental variations (26) and quantify the seasonal variations in seismic wave velocity.

Our model assumes a homogeneous sandstone scenario for the peninsula, based on the findings of the Geological Survey of Japan

(27). We assume the initial hydrostatic equilibrium condition to be in a state of saturation. Each step in the physical model corresponds to a time increment of 30 days. A permeability value of 2500 mD (millidarcy) is used, corresponding to sandstone. The model incorporates multiple data types including atmospheric pressure, the inflow from precipitation and snow melt, estimated from local meteorological station observations, as well as the recorded sea-level fluctuations from the regional Wajima tidal gauge station (Fig. 3B). The average annual variation in sea level exceeds half a meter, and these changes also exert pressure on the coast, resulting in variations in excess pore fluid pressure (28). In regions with substantial snowfall, it is important to consider both the effects of snow loading and melted snow runoff. Figure 3A illustrates the simulated excess pore pressure across the Noto Peninsula in December 2023, with a mesh resolution of 1000 and 500 m in the horizontal and vertical directions, respectively.

The depth of changes in seismic velocity locates approximately to the upper crust based on the theoretical depth sensitivity kernel of coda waves (fig. S3) (9, 29). Seasonal effects are governed by changes in the medium within shallow strata, given that seasonal seismic velocity changes from both measurement periods exhibit a similar change. We therefore plot the simulated excess pore pressure at a depth of 1 km and the seismic velocity time series, averaged over the time series after removing the linear trend from the SUZH-YGDH and YGDH-UCUH station pairs within the 4- to 10-s period range (Fig. 3C).

The correlation between seasonal changes in seismic velocity and excess pore pressure in Fig. 3C is strongly negative, with a coefficient of -0.7 and a stress sensitivity of $6 \times 10^{-9} \text{ Pa}^{-1}$, defined as the ratio between the observed changes in seismic velocity and the modeled

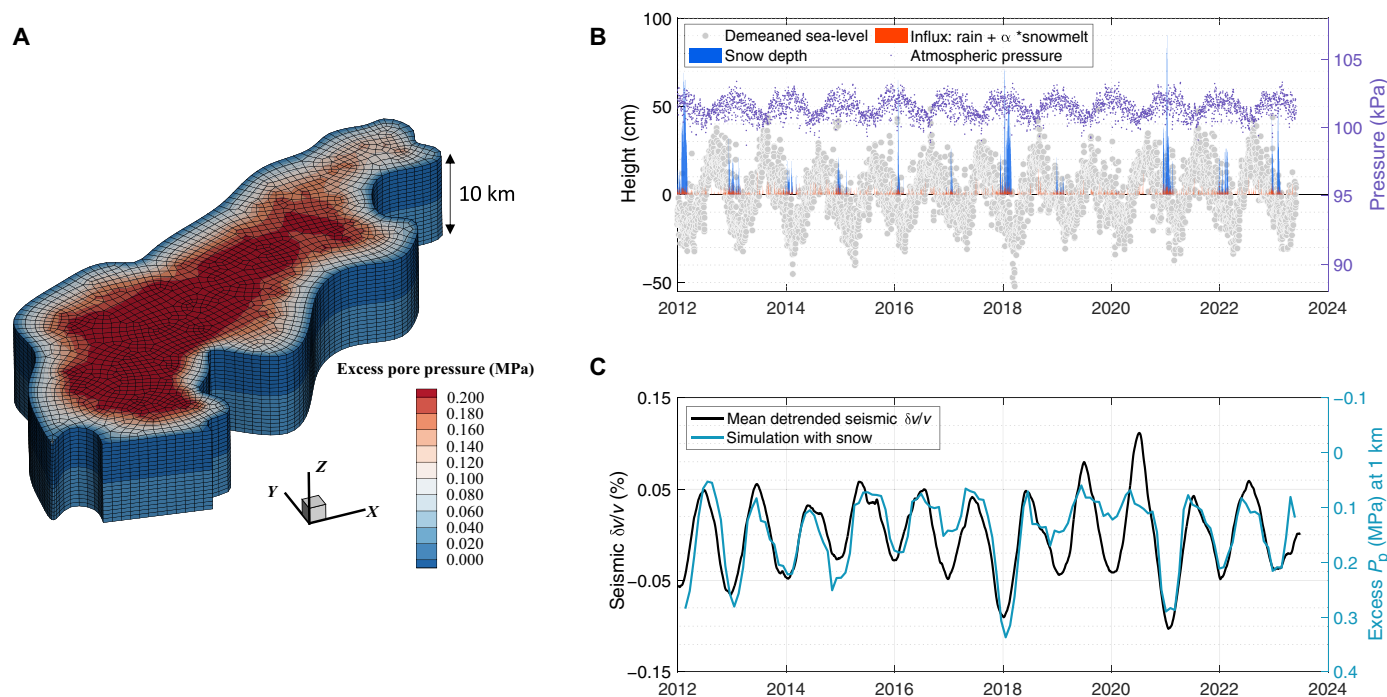


Fig. 3. Modeled evolution of excess pore pressure (megapascals) at 1 km and seismic velocity changes (%) beneath the Noto Peninsula. (A) Model geometry and simulated excess pore pressure in December 2023. **(B)** Local meteorological and oceanographic daily recordings, which include converted water influx, snow depth, atmospheric pressure, and demeaned sea level. **(C)** Comparison between time series of seismic wave velocity captured at 4 to 10 s and modeled excess pore pressure (megapascals).

excess pore pressure. As the excess pore pressure increases, the effective stress, estimated as $\sigma_e = \sigma_n - P_p$, decreases (30), resulting in a decrease in seismic wave velocity (31). Conversely, when the excess pore pressure decreases, it leads to a rebound in seismic wave velocity.

We simulate changes in excess pore pressure both with and without the consideration of snow effects due to loading and snow melt runoff for comparison (fig. S6). Both sets of simulated excess pore pressure values exhibit a similar negative correlation with changes in seismic velocity, but including snow loading and runoff improves the negative correlation by 10%. We see the impact of snow specifically in the years 2013, 2018, and 2021, suggesting that including snow effects is necessary to properly model the subsurface pore pressure.

Seismic velocity drop at the initiation of the Noto earthquake swarm sequences

We observe in the time series of seismic velocity changes from station pair YGDH-SUZH (4 to 10 s), shown in Fig. 4, strong seasonal effects with a long-term increase in seismic velocity before 2020, followed by a rapid decline in late 2020. Similar to the seismic measurements, the GPS time series of vertical displacement from station J253 (part of the Japanese GPS Earth Observation Network) (32, 33) also exhibits strong seasonal effects (34) and a long-term change with subsidence and uplift before and during the swarm, respectively. In the pre-swarm period, the long-term subsidence from ~2014 in the geodetic data coincides with the long-term increase in seismic velocity as observed in Fig. 4. Subsidence in vertical displacement is usually associated with water removal, such as the

compaction of aquifer systems caused by groundwater withdrawals (35) and drainage processes (36), implying that groundwater depletion also results in an increase in seismic velocity. In addition, it may result from sediment consolidation or even slow fault movement (36). Determining the primary cause for this change remains challenging. However, we conclude the presence of linear increase in seismic velocity across the observational region, as evidenced by a consistent linear trend (fig. S7) observed in all seismic velocity change time series.

In the immediate period preceding the intense burst of the earthquake swarms, there is a decrease in seismic wave velocity, indicated by the vertical arrow in Fig. 4A, which is accompanied by a distinct vertical uplift. A systematic analysis using all available GPS stations (2) suggests an uplift of ~70 mm around the source of the earthquake swarm. The abnormal decrease in seismic wave velocity is observable solely in the 4- to 10-s period monitoring results, but not in the 2- to 4-s period. This finding allows us to infer that the decrease in seismic velocity can be attributed to the subsurface deformation at depths likely greater than 8 km, the depth extent of the short-period frequency band (fig. S3). Our observations thus suggest that both seismic and geodetic time series are under the combined influence of tectonic forces (8), environmental forces generated by environmental effects (11, 18, 37).

We isolate the long-term seismic velocity changes first using model regression by assuming a linear relationship between the excess pore pressure and the seasonal effects. While the model effectively simulates the averaged annual patterns of seismic velocity changes (Fig. 3C) between station pairs, residual seismic velocity changes from a single pair, after removing the modeled

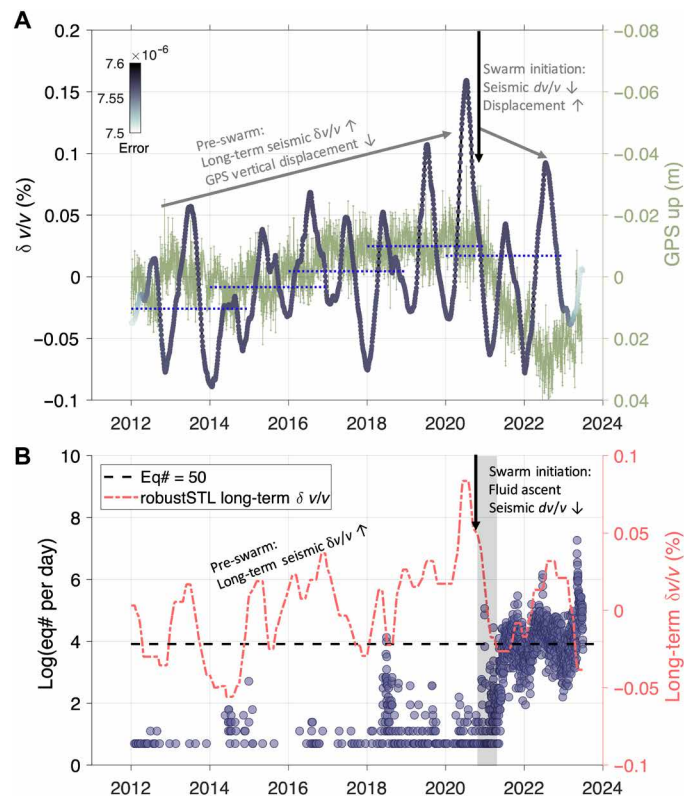


Fig. 4. Time series of seismic velocity changes, vertical displacement, and seismicity. (A) Evolution of seismic velocity changes (with inversion error scatters) between station pairs YGDH and SUZH (4 to 10 s) and demeaned GNSS vertical displacement (station J253). The y axis of vertical displacement is reversed for comparison. The horizontal dotted lines represent averages over 3 years with 1-year overlap. (B) Purple scatter points represent logged daily earthquake numbers. The pink line indicates the long-term trend extracted from the raw $\delta v/v$ time series with robustSTL. Abnormal seismic velocity decreases are observed during the shaded time period.

time series (fig. S9), still exhibit seasonal interference. This is possibly due to variations in local-scale environmental parameters and crustal diffusion rates. The model correction results may lead to improper interpretation. We therefore apply the Robust Seasonal and Trend decomposition using Loess (robust-STL) (38) to empirically decompose the seasonal modulation from the seismic velocity time series. The RobustSTL approach offers the additional advantage of capturing a nonuniform annual pattern, enabling us to reproduce time-variable amplitudes of the seasonal modulation. Both the residuals from the physical and empirical approaches (fig. S9) show comparable results, with a change in seismic velocity for the period before and after swarm periods. We also check the time series of seismic velocity changes using autocorrelation from stations SUZH and YGDH, separately (fig. S10B) to confirm the observed changes in this area. The long-term trends show identical seismic velocity changes (fig. S10C). There is a long-term increase (Fig. 4B and fig. S9) in seismic velocity observed before late 2020, followed by a relatively rapid decrease over ~6 months, as highlighted by the shaded bar in Fig. 4B. This decrease coincides with the period from the onset of the earthquake swarm until the daily number of earthquakes tends to stabilize.

DISCUSSION

Seismic monitoring results show that seasonal effects are present in both short- and long-period seismic velocity changes, explaining a significant amount of their variance. We model the environmental forcings (Fig. 3) by integrating local environmental factors of atmospheric pressure, sea level, snow, and rainfall. The high negative correlation between changes in modeled excess pore pressure and the averaged seasonal effects (Fig. 3C) demonstrate the environmental impacts on the elastic properties of subsurface medium, directly affecting seismic wave velocities and dominating the shallow seismic velocity changes.

Beyond the seasonal effects, we have isolated long-term seismic velocity changes measured at long period that are coincident with vertical surface displacement (Fig. 4). The gradual decrease in seismic velocity lasting ~6 months is simultaneous with the early stage of the swarm, from the initiation of seismicity to the intense, sustained sequence of seismic events. The local seismic structure (6) shown in Fig. 5 features a high V_p/V_s zone ~25 km beneath the swarm zone that suggests a high-pore fluid pressure environment (39). We suggest that, once faults within and above this zone are destabilized (Fig. 5A), the high pore fluid pressure will ascend and perturb the stress state of preexisting faults or fractures. Increasing pore fluid pressure throughout the swarm source region will decrease fault strength and initiate seismic events in the critically stressed crust above (40, 41). We therefore interpret the observed decrease in seismic wave velocity (Fig. 4B) to reveal this diffusion process (42, 43), driven from the high-pore fluid pressure zone upward to the seismogenic zone (44) where preexisting reverse faults are present. If we consider that high fluid pressure diffuses from ~25-km depth and migrates 10 km upward into the earthquake swarm source region over ~6 months (Fig. 4B), then the estimated diffusion rate is $\sim 0.51 \text{ m}^2/\text{s}$, based on the isotropic pore fluid pressure diffusion model $R = \sqrt{4\pi Dt}$ (45). This rate of diffusion closely matches other recent estimates ranging from 0.5 to $1 \text{ m}^2/\text{s}$ that were derived from the migration of the earthquake catalog itself (4). The swarm then continued (Fig. 5, red dots) as the high pore pressure migrates within a network (46) of preexisting reverse faults.

As shown in Fig. 5A, our model highlights a notable increase in excess pore pressure of more than 20 kPa at a depth of 9 km during 2018 and 2021. This increase was subsequently accompanied by clusters of earthquakes, both short-lived and sustained, in the swarm source region. The relative high excess pore pressure resulting from intense periods of snow fall and subsequent hydrological loading will persist, even with alterations in permeability and porosity for modeling. We suggest that this environmental forcing affected pore fluid pressures at depth and acted to destabilize preexisting fractures within a fluid-saturated fault zone (4). Thus, the high excess pore pressure resulting from the substantial snow depth as observed during the winters of 2018 and 2021 likely triggered the diffusive fluid ascent by activating fractures. This diffusive process controls the timescale between the peak of excess pore pressure, which is dominated by the accumulation of snow on the surface, and the burst of earthquake clusters. Intense snow fall can potentially act as a trigger factor in an analogous fashion to the seasonal modulation of seismicity in the Himalaya by monsoon rains (47), climate-driven surface uplift (48, 49), rainfall-triggered earthquake activity (50), and fault reactivation triggered by the climate-induced melting of large ice sheets in central Europe (51).

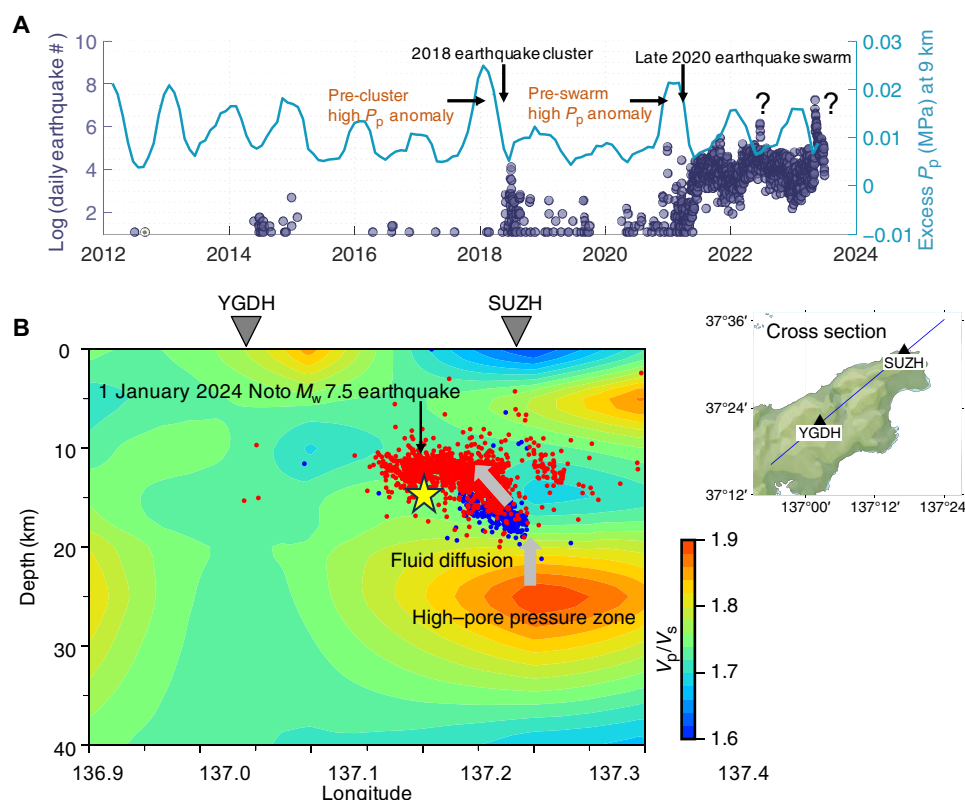


Fig. 5. Schematic evolution of the subsurface before and during the Noto earthquake swarm. (A) Modeled evolution of pore pressure (megapascals) at 9-km depth. Two abnormal high-pore pressure (P_p) values in 2018 and 2021 precede an earthquake cluster and the ongoing earthquake swarm, respectively. (B) Gross spatiotemporal migration of earthquakes in the Noto swarm overlaid on seismic V_p/V_s structure (δ) along the cross section passing through the two seismic stations. Colored dots represent seismic activity in January 2021 (blue, example for the initial stage) and July 2021 (red, example for the following stage), highlighting the dynamic changes in seismic event locations over time.

Besides the 2018 earthquake cluster and the initiation of the late 2020 earthquake swarm, we highlight further earthquake clusters in 2022 and 2023 that follow peaks of high excess pore pressure, as indicated by the question marks in Fig. 5A. In addition, the recent earthquake with moment magnitude (M_w) of 7.5 on New Year's Day of 2024 (yellow star in Fig. 5B), followed by a rapid extension of aftershocks in a similar direction along the YGDH-SUZH pair in this nontypical subduction zone, occurred within the swarm source zone. Whether these events result from a similar fluid diffusion process triggered by snow remains uncertain. This hypothesis requires further investigation with a more comprehensive earthquake catalog that includes improved earthquake detection and location for a statistical analysis.

We demonstrate here how seismic interferometry serves as a robust tool for tracking and assessing subsurface deformation. When exploring what factors can alter the stress state of the seismogenic subsurface, it is indispensable to consider external forces originating from environmental perturbations, internal tectonic forcings, and the variations in fluid pressure that link them together. The seasonal subsurface deformation can be effectively explained by the combined influences of environmental factors using our hydromechanical model. Snow, in particular, plays multiple roles in altering the subsurface excess pore pressure and, consequently, the effective stress. In addition, rising or extreme temperatures can lead to sea-level

changes, which may generate long-term ocean loading changes (52) and can also contribute to the stress changes in the coastal region. By taking into account these factors, we can physically model and interpret the observed complex seasonal effects, which evolve with time, to gain valuable insights into how these external forces may alter crustal stresses and potentially trigger seismic rupture.

MATERIALS AND METHODS

Earthquake catalog

The earthquake catalog (Fig. 1A) used in this study is sourced from the JMA's automatic detection system, which provides provisional information regarding seismic events in the region. We analyze this catalog following the work by (20, 21). We calculate time histogram of seismic activity, counting the number of earthquakes in regularly spaced time bins of 1 min. We then compute the power spectral density of this earthquake count time series (fig. S1) for two distinct time periods: before (2012 to 2018) and during earthquake swarm periods (after 2021). The swarm period exhibits an increase of power with increasing period, indicating that the earthquake timing is correlated and statistically clustered in time, while the power spectrum of earthquake occurrence during the pre-swarm period is flat, suggesting that the events are uncorrelated.

Preparation of meteorological data and other observations

For environmental recordings, we use sea-level data recorded by the regional Wajima tidal gauge station (Fig. 1A). The annual difference in sea-level between winter and summer is more than 0.5 m per year. With this information, we are able to examine how sea-level changes may affect the coastal region through our modeling effort. In addition, we gather climate data from a nearby meteorological station (Fig. 1A), which records daily measurements of precipitation, snow depth, and snowfall. This meteorological data enabled us to investigate the influence of environmental conditions on changes in seismic velocity, thereby aiding our understanding of subsurface deformation processes.

We calculate snowmelt from two observations: One is the snow depth difference $\Delta d(i)_1$ between the current day $d(i)$ and the previous day $d(i - 1)$ for temperatures equal to or below 0°C, and the other is the difference $\Delta d(i)_2$ between the current snowfall and the increase in snow depth $d(i)$ compared to day $i - 1$. The total snowmelt is equal to $\alpha \cdot [\Delta d(i)_1 + \Delta d(i)_2]$, where α is the snow-water-equivalent coefficient. We assume α to be a constant with an average value of 0.3 (53).

In addition, we incorporate vertical surface displacement data from a nearby GNSS station, which provides complementary information to the seismic observations and captures long-term deformation processes associated with the ongoing earthquake swarm. To study both long-term and transient changes, all of these continuous datasets span an 11-year period, covering the initiation of the earthquake swarm up to the present. This extended timeframe has enabled us to detect and analyze long-term variations in subsurface deformation, facilitating a comprehensive examination of the underlying factors driving the Noto earthquake swarm.

Measurement of time series of seismic velocity changes

We gather continuous seismic data from the vertical component of three seismic stations located in close proximity to the earthquake swarm. To improve the stability of the noise records before correlation, we first remove the earthquake events by time-domain clipping to remove the main high-frequency spikes and glitches (54) and then apply 1-bit normalization and spectral whitening in the band from 0.08 to 2.0 Hz. We calculate continuous cross-correlation functions for 20-min seismic signal segments and then stack the cross-correlation functions for each 3-day period and monitor the time series of seismic velocity changes by through coda wave interferometry (8).

For the phase-shift measurements, we use the doublet method (55) and measure the travel-time differences between any two correlation functions and then invert the phase differences to a time series of seismic velocity changes. The measurement considers two period ranges: 2 to 4 s and 4 to 10 s to investigate different depths of seismic velocity changes. The time series of seismic velocity changes from the three station pairs exhibit seasonal patterns that are in phase with a decrease during winter and an increase during summer, for both the 2- to 4-s and 4- to 10-s period ranges.

Physical model building

A 3D fully coupled thermal-hydromechanical simulator HENGYI (26) is used in this study to simulate the pore pressure evolution underneath the Noto Peninsula from 2012 until 2023. We define the

3D geometry of the model by tracing the outline of the Noto Peninsula in map view and then sweeping the outline in the vertical direction by 10 km. The model is cutoff along 37°07'N, which is enough far away from the seismic record stations to avoid the influence of boundary conditions. Unstructured hexahedron elements are used to mesh the model with a resolution of ~1000 m in the horizontal directions and 500 m in the vertical direction.

In terms of boundary conditions, rainfall and snow melt are imposed as fluid influx over the entire top surface of the model. The upper 5 km of the lateral boundaries is subject to hydrostatic pressure fluctuating with sea level. No change in hydrostatic pressure is considered for the rest of the boundaries. For the mechanical boundary conditions, the remainder of the snow is applied to the top surface as pressure loading due to self-weight. Atmospheric pressure is also exerted to the top surface according to the local meteorological records. The bottom surface is fixed in all directions (i.e., zero displacement). The horizontal movement of the cutoff plane is prohibited, while its vertical displacement is allowed to simulate ground uplift or subsidence. The rest of the boundaries are free to deform. For the initial conditions, the rock mass is considered to be saturated with hydrostatic pore pressure. The temperature variable is not included in the present simulation; thus, only the hydro-mechanical part of the thermal-hydromechanical is active.

For the material parameters, according to the geological condition of Japan (27), the Noto Peninsula is mainly constituted by sedimentary rocks. Here, we use the mechanical and hydraulic parameters of typical sandstone to perform the simulation. The elastic modulus, Poisson's ratio, and permeability of the rock mass are 20 GPa, 0.3, and 2500 mD, respectively. The simulated duration is 11 years with a constant time step of 30 days. After simulation, the excess pore pressure (pore pressure minus hydrostatic pressure) history in the middle part of the Noto Peninsula is extracted and plotted in Fig. 3C against the seismic wave velocity.

The comparison of model results at different locations, using different permeability, and the comparison between the model with and without snow are shown in the Supplementary Materials in figs. S4 to S6. The amplitude of excess pore pressure may vary at different locations, while the phase does not differ significantly, as we consider a uniform model. The model without snow shows less correlation compared to the model with snow, highlighting the importance of considering snow for studying the subsurface deformation.

Time-series decomposition

We apply RobustSTL (38), functional fitting, and physical model correction to decompose the velocity change time series for comparing seasonal signals and isolating long-term changes. RobustSTL uses the least absolute deviation loss with sparse regularization to address regression problems. We consider an annual seasonal effect, sampling one past season and two neighboring seasons for seasonality extraction. This approach enables us to mathematically extract the underlying seasonal signals and trends from the time-series data. It has actively showcased its efficiency in decomposing irregular seasonal components and adeptly addressing abrupt and level changes in trend signals, precisely the areas that we aimed to target.

We also assume a linear relationship between seismic velocity changes and modeled excess pore pressure changes, which are based on environmental factors. First, we remove the linear trend from the raw time series of seismic velocity changes. Then, we obtain the

model time series of seismic velocity changes through linear regression. The long-term trend is calculated as the difference between the raw and the modeled time series of seismic velocity changes.

Supplementary Materials

This PDF file includes:

Figs. S1 to S10

Equations S1 and S2

References

REFERENCES AND NOTES

- J. E. Vidale, P. M. Shearer, A survey of 71 earthquake bursts across southern California: Exploring the role of pore fluid pressure fluctuations and aseismic slip as drivers. *J. Geophys. Res. Solid Earth* **111**, B05312 (2006).
- T. Nishimura, Y. Hiramatsu, Y. Ohta, Episodic transient deformation revealed by the analysis of multiple GNSS networks in the Noto Peninsula, central Japan. *Sci. Rep.* **13**, 8381 (2023).
- Y. Amezawa, Y. Hiramatsu, A. Miyakawa, K. Imanishi, M. Otsubo, Long-living earthquake swarm and intermittent seismicity in the northeastern tip of the Noto Peninsula, Japan. *Geophys. Res. Lett.* **50**, e2022GL102670 (2023).
- K. Yoshida, M. Uno, T. Matsuzawa, Y. Yukutake, Y. Mukuhira, H. Sato, T. Yoshida, Upward earthquake swarm migration in the northeastern Noto Peninsula, Japan, initiated from a deep ring-shaped cluster: Possibility of fluid leakage from a hidden magma system. *J. Geophys. Res. Solid Earth* **128**, e2022JB026047 (2023).
- K. Yoshida, N. Uchida, Y. Matsumoto, M. Orimo, T. Okada, S. Hirahara, S. Kimura, R. Hino, Updip fluid flow in the crust of the northeastern Noto Peninsula, Japan, triggered the 2023 M_w 6.2 suzu earthquake during swarm activity. *Geophys. Res. Lett.* **50**, e2023GL106023 (2023).
- J. Nakajima, Crustal structure beneath earthquake swarm in the Noto Peninsula, Japan. *Earth Planets Space* **74**, 160 (2022).
- J. Doetsch, V. S. Gischig, L. Villiger, H. Krietsch, M. Nejati, F. Amann, M. Jalali, C. Madonna, H. Maurer, S. Wiemer, D. Driesner, D. Giardini, Subsurface fluid pressure and rock deformation monitoring using seismic velocity observations. *Geophys. Res. Lett.* **45**, 10389–10397 (2018).
- F. Brenguier, M. Campillo, T. Takeda, Y. Aoki, N. M. Shapiro, X. Briand, K. Emoto, H. Miyake, Mapping pressurized volcanic fluids from induced crustal seismic velocity drops. *Science* **345**, 80–82 (2014).
- A. Obermann, B. Froment, M. Campillo, E. Larose, T. Planès, B. Valette, J. H. Chen, Q. Y. Liu, Seismic noise correlations to image structural and mechanical changes associated with the M_w 7.9 2008 wenchuan earthquake. *J. Geophys. Res. Solid Earth* **119**, 3155–3168 (2014).
- Q.-Y. Wang, M. Campillo, F. Brenguier, A. Lecointre, T. Takeda, A. Hashima, Evidence of changes of seismic properties in the entire crust beneath Japan after the M_w 9.0, 2011 Tohoku-oki earthquake. *J. Geophys. Res. Solid Earth* **124**, 8924–8941 (2019).
- P. Poli, V. Marguin, Q.-Y. Wang, N. D'Agostino, P. Johnson, Seasonal and coseismic velocity variation in the region of L'Aquila from single station measurements and implications for crustal rheology. *J. Geophys. Res. Solid Earth* **125**, e2019JB019316 (2020).
- Y. Lu, Y. Ben-Zion, Regional seismic velocity changes following the 2019 M_w 7.1 ridgecrest, california earthquake from autocorrelations and P/S converted waves. *Geophys. J. Int.* **228**, 620–630 (2022).
- T. Clements, M. A. Denolle, The seismic signature of California's earthquakes, droughts, and floods. *J. Geophys. Res. Solid Earth* **128**, e2022JB025553 (2023).
- T. Hirose, Q.-Y. Wang, M. Campillo, H. Nakahara, L. Margerin, E. Larose, T. Nishimura, Time-lapse imaging of seismic scattering property and velocity in the northeastern japan. *Earth Planet. Sci. Lett.* **619**, 118321 (2023).
- L. A. Ermert, E. Cabral-Cano, E. Chaussard, D. Solano-Rojas, L. Quintanar, D. Morales Padilla, E. A. Fernández-Torres, M. A. Denolle, Probing environmental and tectonic changes underneath Mexico city with the urban seismic field. *Solid Earth* **14**, 529–549 (2023).
- F. Xie, E. Larose, Q.-Y. Wang, Y. Zhang, In-situ monitoring of rock slope destabilization with ambient seismic noise interferometry in southwest china. *Eng. Geol.* **312**, 106922 (2023).
- F. Brenguier, M. Campillo, C. Hadzioannou, N. M. Shapiro, R. M. Nadeau, E. Larose, Postseismic relaxation along the san andreas fault at parkfield from continuous seismological observations. *Science* **321**, 1478–1481 (2008).
- Q.-Y. Wang, "Monitoring of the mechanical properties of the crust beneath Japan from continuous data of the Hi-net network," thesis, Université Grenoble Alpes (2018).
- J. Dieterich, A constitutive law for rate of earthquake production and its application to earthquake clustering. *J. Geophys. Res. Solid Earth* **99**, 2601–2618 (1994).
- W. B. Frank, B. Rousset, C. Lasserre, M. Campillo, Revealing the cluster of slow transients behind a large slow slip event. *Sci. Adv.* **4**, eaat0661 (2018).
- W. B. Frank, N. M. Shapiro, A. A. Gusev, Progressive reactivation of the volcanic plumbing system beneath tolbachik volcano (Kamchatka, Russia) revealed by long-period seismicity. *Earth Planet. Sci. Lett.* **493**, 47–56 (2018).
- K. Obara, K. Kasahara, S. Hori, Y. Okada, A densely distributed high-sensitivity seismograph network in Japan: Hi-net by National Research Institute for Earth Science and Disaster Prevention. *Rev. Sci. Instrum.* **76**, 021301 (2005).
- NIED Hi-net, National Research Institute for Earth Science and Disaster Resilience (2019).
- Q.-Y. Wang, F. Brenguier, M. Campillo, A. Lecointre, T. Takeda, Y. Aoki, Seasonal crustal seismic velocity changes throughout Japan. *J. Geophys. Res. Solid Earth* **122**, 7987–8002 (2017).
- M. Ozaki, "1:200,000 geological map of the northern part of Noto Peninsula" in *Seamless Geoinformation of Coastal Zone "Northern Coastal Zone of Noto Peninsula"* (Digital Geoscience Map S-1, 2010), P013.
- X. Cui, L. N. Y. Wong, A 3d fully thermo-hydro-mechanical coupling model for saturated poroelastic medium. *Comput. Methods Appl. Mech. Eng.* **394**, 114939 (2022).
- K. Wakita, Geology and tectonics of Japanese islands: A review - The key to understanding the geology of asia. *J. Asian Earth Sci.* **72**, 75–87 (2013).
- N. Sultan, A. Plaza-Faverola, S. Vadakkupuliyambatta, S. Buenz, J. Knies, Impact of tides and sea-level on deep-sea arctic methane emissions. *Nat. Commun.* **11**, 5087 (2020).
- L. Margerin, A. Bajaras, M. Campillo, A scalar radiative transfer model including the coupling between surface and body waves. *Geophys. J. Int.* **219**, 1092–1108 (2019).
- M. Rempe, G. Di Toro, T. M. Mitchell, S. A. F. Smith, T. Hirose, J. Renner, Influence of effective stress and pore fluid pressure on fault strength and slip localization in carbonate slip zones. *J. Geophys. Res. Solid Earth* **125**, e2020JB019805 (2020).
- M. Landrø, Discrimination between pressure and fluid saturation changes from time-lapse seismic data. *Geophysics* **66**, 836–844 (2001).
- T. Sagiya, A decade of GEONET: 1994–2003–The continuous GPS observation in Japan and its impact on earthquake studies. *Earth Planet Space* **56**, xxix–xli (2004).
- G. Blewitt, W. C. Hammond, C. Kreemer, Harnessing the GPS data explosion for interdisciplinary science. *Eos* **99**, 1–2 (2018).
- K. Heki, Seasonal modulation of interseismic strain buildup in northeastern Japan driven by snow loads. *Science* **293**, 89–92 (2001).
- H. Abidin, H. Andreas, R. Djaja, D. Darmawan, M. Gamal, Land subsidence characteristics of jakarta between 1997 and 2005, as estimated using GPS surveys. *GPS Solut* **12**, 23–32 (2008).
- T. A. Meckel, U. S. ten Brink, S. J. Williams, Current subsidence rates due to compaction of holocene sediments in southern louisiana. *Geophys. Res. Lett.* **33**, L11403 (2006).
- R. Kramer, Y. Lu, G. Bokelmann, Interaction of air pressure and groundwater as main cause of sub-daily relative seismic velocity changes. *Geophys. Res. Lett.* **50**, e2022GL101298 (2023).
- Q. Wen, J. Gao, X. Song, L. Sun, H. Xu, S. Zhu, RobustSTL: A robust seasonal-trend decomposition algorithm for long time series. arXiv:1812.01767 [cs, eess, stat] (2018).
- P. Audet, M. G. Bostock, N. I. Christensen, S. M. Peacock, Seismic evidence for overpressured subducted oceanic crust and megathrust fault sealing. *Nature* **457**, 76–78 (2009).
- A. Nur, J. R. Booker, Aftershocks caused by pore fluid flow? *Science* **175**, 885–887 (1972).
- Q.-Y. Wang, W. B. Frank, R. E. Abercrombie, K. Obara, A. Kato, What makes low-frequency earthquakes low frequency. *Sci. Adv.* **9**, eadh3688 (2023).
- Q. Y. Wang, M. Campillo, F. Brenguier, A. Lecointre, T. Takeda, K. Yoshida, Seismic evidence of fluid migration in northeastern Japan after the 2011 Tohoku-Oki earthquake. *Earth Planet. Sci. Lett.* **563**, 116894 (2021).
- T. Tonegawa, S. Takemura, S. Yabe, K. Yomogida, Fluid migration before and during slow earthquakes in the shallow nankai subduction zone. *J. Geophys. Res. Solid Earth* **127**, e2021JB023583 (2022).
- V. M. Cruz-Atienza, C. Villafuerte, H. S. Bhat, Rapid tremor migration and pore-pressure waves in subduction zones. *Nat. Commun.* **9**, 2900 (2018).
- S. A. Shapiro, E. Huenges, G. Borm, Estimating the crust permeability from fluid-injection-induced seismic emission at the ktb site. *Geophys. J. Int.* **131**, F15–F18 (1997).
- R. H. Sibson, Structural permeability of fluid-driven fault-fracture meshes. *J. Struct. Geol.* **18**, 1031–1042 (1996).
- L. Bollinger, F. Perrier, J.-P. Avouac, S. Sapkota, U. Gautam, D. R. Tiwari, Seasonal modulation of seismicity in the himalaya of nepal. *Geophys. Res. Lett.* **34**, L08304 (2007).
- K. Compton, R. A. Bennett, S. Hreinsdóttir, Climate-driven vertical acceleration of icelandic crust measured by continuous gps geodesy. *Geophys. Res. Lett.* **42**, 743–750 (2015).

49. R. B. Bürgmann, K. Chanard, Y. Fu, Climate- and weather-driven solid-earth deformation and seismicity. *EarthArXiv* (2023).
50. S. Hainzl, T. Kraft, J. Wassermann, H. Igel, E. Schmedes, Evidence for rainfall-triggered earthquake activity. *Geophys. Res. Lett.* **33**, L19303 (2006).
51. C. Brandes, H. Steffen, R. Steffen, P. Wu, Intraplate seismicity in northern Central Europe is induced by the last glaciation. *Geology* **43**, 611–614 (2015).
52. S. R. McNutt, R. J. Beavan, Eruptions of pavlof volcano and their possible modulation by ocean load and tectonic stresses. *J. Geophys. Res. Solid Earth* **92**, 11509–11523 (1987).
53. M. Sturm, B. Taras, G. E. Liston, C. Derksen, T. Jonas, J. Lea, Estimating snow water equivalent using snow depth data and climate classes. *J. Hydrometeorol.* **11**, 1380–1394 (2010).
54. P. Boué, P. Roux, M. Campillo, X. Briand, Phase velocity tomography of surface waves using ambient noise cross correlation and array processing. *J. Geophys. Res. Solid Earth* **119**, 519–529 (2014).
55. G. Poupinet, W. L. Ellsworth, J. Frechet, Monitoring velocity variations in the crust using earthquake doublets: An application to the calaveras fault, california. *J. Geophys. Res. Solid Earth* **89**, 5719–5731 (1984).
56. J. Quilty, J. Adamowski, A maximal overlap discrete wavelet packet transform integrated approach for rainfall forecasting - A case study in the Awash River Basin (Ethiopia). *Environ. Model. Softw.* **144**, 105119 (2021).

Acknowledgments: We thank J. Nakajima for the seismic tomography results in the study region. **Funding:** Q.-Y.W. acknowledges support from the International Research Fellow of Japan Society for the Promotion of Science no. 33-11-21. W.B.F and Q.-Y.W. acknowledge support from the National Science Foundation under EAR award no. 2103408. **Author contributions:** Conceptualization: Q.-Y.W., W.B.F., and K.O. Methodology: Q.-Y.W., X.C., and Y.L. Visualization: All authors. Funding acquisition: Q.-Y.W. and W.B.F. Writing—original draft: Q.-Y.W. Writing—review and editing: All authors. **Competing interests:** The authors declare that they have no competing interests. **Data and materials availability:** All data needed to evaluate the conclusions in the paper are present in the paper and/or the Supplementary Materials. Hi-net seismic data required in the paper are available from the National Research Institute for Earth Science and Disaster Prevention (NIED; www.hinet.bosai.go.jp). The earthquake catalogs used in the paper are available from the Japan Meteorological Agency (JMA; www.data.jma.go.jp/svd/eqev/data/bulletin/catalog/notes_e.html).

Submitted 18 January 2024

Accepted 4 April 2024

Published 8 May 2024

10.1126/sciadv.ado1469